Physical and Radiative Characteristics and Long Term Variability of the Okhotsk Sea Ice Cover

Fumihiko Nishio[1], Josefino C. Comiso[2], Robert Gersten[3,2], Masashige Nakayama[4], Jinro Ukita[1], Al Gasiewski[5], Boba Stanko[5], and Kazuhiro Naoki[1]

[1]Center for Environmental Remote Sensing, Chiba University, 1-33 Yayoi-cho, Inage-ku, Chiba City

[2]Cryosphere Sciences Branch, NASA Goddard Space Flight Center, Greenbelt, MD 20771

[3]RSIS, Greenbelt, MD 20770

[4]Hokkaido Ice Musuem, Hokkaido, Japan

[5]NOAA Environmental Research Laboratory, 325 Broadway Ave., Boulder, Colorado, 80303

Submitted to JGR-Oceans

as part of the special section on

"Large Scale Characteristics of the Sea Ice Cover using AMSR-E and other Satellite Data"

Abstract

Much of what we know about the large scale characteristics of the Okhotsk Sea ice cover has been provided by ice concentration maps derived from passive microwave data. To understand what satellite data represent in a highly divergent and rapidly changing environment like the Okhotsk Sea, we take advantage of concurrent satellite, aircraft, and ship data acquired on 7 February and characterized the sea ice cover at different scales from meters to hundreds of kilometers. Through comparative analysis of surface features using co-registered data from visible, infrared and microwave channels we evaluated the general radiative and physical characteristics of the ice cover as well as quantify the distribution of different ice types in the region. Ice concentration maps from AMSR-E using the standard sets of channels, and also only the 89 GHz channel for optimal resolution, are compared with aircraft and high resolution visible data and while the standard set provides consistent results, the 89 GHz provides the means to observe mesoscale patterns and some unique features of the ice cover. Analysis of MODIS data reveals that thick ice types represents about 37% of the ice cover indicating that young and new ice types represent a large fraction of the ice cover that averages about 90% ice concentration according to passive microwave data. These results are used to interpret historical data that indicate that the Okhotsk Sea ice extent and area are declining at a rapid rate of about -9% and -12 % per decade, respectively.

1. Introduction

The Okhotsk Sea has the unique distinction of being the southernmost region in the Northern Hemisphere with sea ice cover. The variability of the sea ice cover is thus sometimes linked closely to the changing climate of the region. It is also among the world's most productive and richest fishing grounds, in part because of the presence of sea ice during the winter and spring period. With its high productivity, it is also regarded as a potential carbon sink. Satellite data revealed the existence of latent as well as sensible heat polynyas that can have considerable impacts on the physical characteristics of the sea (Alfultis and Martin, 1987). Furthermore, sea ice is an integral part of the culture and lives of inhabitants in the coastal regions that surround the sea as manifested

63 by the existence of several communities along the coastlines and radar stations for
64 monitoring the ice cover for several decades (e.g., Mombetsu, Japan). Such coverage,
65 however has been limited and it was not until the advent of satellite remote sensing that
66 the true nature and extent of the sea ice in the region was revealed. During the satellite
67 era, large interannual variability and significant decline has been observed (Parkinson et
68 al., 1999) while anomalies in some years have been associated with El Nino events
69 (Nishio et al., 1998). A recovery was observed in 2001 but from that time on, the ice
70 cover has been declining again.
71 Among the objectives of this study is to utilize data concurrently observed from
72 aircraft, ship, and sensors from different or the same satellite platforms during the 2003
73 winter season to provide as comprehensive a characterization of the sea ice cover in the
74 Okhotsk Sea as possible. Of special interest is the spatial distribution of the different ice
75 types, especially the different types of new and young ice as well as the thick first year
76 ice. The strategy is to start with the large scale characteristics as can be inferred from ice
77 concentration maps derived from passive microwave data. The ice concentration maps
78 are in turn compared with high resolution satellite data in the visible and infrared to
79 obtain a general idea how the mesoscale distributions of sea ice is represented in these
80 ice concentration maps. High resolution aircraft microwave data are analyzed
81 concurrently with high resolution visible and infrared data to better understand the
82 passive microwave signature of ice in the region and how and why the derived ice
83 concentration varies significantly within the pack. These results are in turn used to
84 interpret the large scale seasonal and interannual variablity as observed from passive
85 microwave data. Long term changes and trends are also examined in the same context
86 with a view of gaining insights into what makes the ice cover in the region so variable.
87
88 **2. The Okhotsk Sea Ice Cover: Large scale and Mesoscale Characteristics**
89
90 *2.1 Satellite Observations*
91 The first Advanced Microwave Scanning Radiometer was launched on board the
92 EOS-Aqua satellite on 4 May 2002 and is called AMSR-E, while the second one, called
93 AMSR, was launched on board the Midori-2 satellite on 24 December 2002. The two

systems have very similar specifications, the biggest difference being that AMSR has an additional 52 GHz channel that is used primarily for atmospheric sounding. Sea ice data from the two have been compared and provide nearly identical results, the difference likely associated with changes due to time difference in the equatorial crossing for the ascending orbits being 13:30 and 22:30 for AMSR-E and AMSR, respectively. AMSR-E is still in operation while the Midori-2/AMSR ceased operation on 23 October 2003 because of satellite hardware problems. The data used in the comparative study are those from AMSR-E, only because AMSR was not in full operation when the aircraft and ship measurements were made. The characteristics of AMSR-E are summarized in Table 1. As indicated, the resolution varies with frequency with the 89 GHz data having the highest resolution at 5.4 km. The sensor scans at a fixed incidence angle of 55° with a swath width of 1445 km covering practically the entire polar region. For long term variability studies, we make use primarily of historical SMMR and SSM/I data for consistency but we take advantage of almost 5 years overlap of SSM/I and AMSR-E to make the data from these two sensors compatible.

The large scale characteristics of the Okhotsk Sea ice cover on 7 February 2003 as depicted by an ice concentration map derived from AMSR-E data is presented in Figure 1. Because of the strong contrast in the emissivity between sea ice and open water, the ice concentration maps provide consistent locations of the ice edges, large divergence areas, and polynyas (e.g., to the north at around 56° N). Because of day/night all weather capabilities, the data is ideal for monitoring large scale seasonal and interannual changes in the ice cover, as will be illustrated below. Several algorithms have been developed to estimate ice concentration using different techniques and sets of channels (Svendsen et al., 1984; Cavalieri et al., 1984; Swift et al., 1986; Comiso, 1986). In this study, we used data derived from the Bootstrap Algorithm as described in Comiso (2004). AMSR-E data at high latitudes have been gridded in polar stereographic format at 12.5 by 12.5 km to take advantage of the improved resolution of the new system. The data have also been gridded at 25 by 25 km resolution for compatibility with historical passive microwave ice data. Furthermore, for studies that require optimal resolution, a special data set with 6.25 by 6.25 km resolution has been generated utilizing only the 89 GHz channels (H&V) and the Bootstrap technique as described in Comiso (2004).

It is fortuitous that on board the Aqua satellite is the Moderate Resolution Imaging Spectroradiometer (MODIS) which is a 36 channel sensor that covers the electromagnetic spectrum from 0.405 to 14.385 μm with spatial resolutions of 1 km at nadir for most channels and at 250 m and 500 m for some special channels. The sensor scans crosstrack with a swath width of 2,330 km for optimal coverage and good temporal resolution in the polar region. The visible channels provides the means to discriminate different surface types including open water, various types of new ice, young ice and thick ice with snow cover during daytime. The thermal channels provide day/night capability and enable estimates of ice concentration as well as the thickness of ice covered surfaces. During clear skies conditions, MODIS provides valuable information about the ice cover and at the same time the means to properly interpret the passive microwave data. The images in Figure 2 shows visible and infrared images from MODIS for the same day. Unfortunately, for that day, only the Terra/MODIS provided good clear sky coverage since by the time Aqua/MODIS passed over the same region four hours later, there were more clouds in the region. The MODIS data, however, provides a good overview of how the sea ice cover look like on that date. Compared to the ice cover as depicted in Figure 1, the images in Figure 2 reveals a lot more details with the visible and infrared channels providing complementary information. In Figure 1, the marginal ice zone is represented by a progression of ice concentrations changing from near 100% to zero % over approximately 100-150 km region. On the other hand, the MIZ is represented by MODIS as consisting mainly of ice bands, the widths of which gets narrower closer to the open sea. With the MODIS data, the unique distributions of different ice types in the region are also more fully revealed. In this sense, the thermal infrared data provide information about the thickness of new ice, especially in lead areas. Figure 3 provides a blown up view of the ice conditions and shows additional details in the coverage and indicating a different pattern in the infrared for consolidated ice (top left) than in the relatively loose ice regions. Patterns of large leads in the top left and thick ice foes in the top middle parts of the image are identified in the image. The presence of snow cover causes surfaces of different ice types to have basically the same albedo but the infrared image is able to capture the distribution of the various ice types with the dark ones representing thick ice floes and the lighter ones representing thinner

ice floes. On the other hand, the banding structure that is revealed in great details in the visible channel (top right) is not captured by the infrared data mainly because the surfaces likely have similar temperatures.

Even more detailed information about the spatial distribution and surface characteristics, of the ice cover can be obtained from Landsat-7data. The Enhanced Thematic Mapper Plus (ETM+) sensor aboard the satellite has a panchromatic band with 15-m resolution and a thermal infrared band at 60-m resolution. For comparison, the highest resolution from a MODIS visible channel is 250 m while that for its infrared band is 1 km. The panchromatic band allows detection of details and improved classification of surface types especially in narrow lead areas. However, the swath width of Landsat is only 185 km while that for MODIS is 2330 km providing much less coverage in a single day. During the aircraft campaign, good Landsat images were obtained on 11 February and some other days but not on 7 February. Thus, comparative studies with aircraft and ship data during the 7 February campaign will be done mainly with MODIS data while the Landsat image of 11 February will be compared with near simultaneous AMSR-E data.

2.2 P3 Aircraft Observations

As part of a dedicated campaign to study the physical and radiative characteristics of the Okhotsk Sea ice cover, we planned two missions using an instrumented NASA P3 aircraft over selected transects in conjunction with a dedicated ship program as described below. The first of these missions was successfully implemented but the second one was not because the aircraft suffered a hardware problem and the latter had to be canceled. The flight track of the first and only mission over the sea is presented together with an ice concentration map derived from AMSR-E data in Figure 1. The aircraft went north from its staging station at the Yokota Airforce Base (near Tokyo) at high altitude (6000), covered a relatively large area (i.e., 175 by 50 km) at the farthest end, for comparative studies with satellite data, as shown, and on the way back it went south at low altitude (1,000 m) to collect data at an even higher resolution. Camera equipments were mounted for high resolution visible coverage but the most important sensor on board the aircraft is the Polarimetric Scanning Radiometer (PSR–A) which has frequency channels from 10 to

89 GHz that matches most of those of the AMSR-E sensor. The field-of-view of the radiometers varies with frequency and at 37 GHz channel, the size of the footprint is about 240 m at the cruising altitude of 6,000 m while it is about 40 m at 1000 m altitude. Data from PSR thus allows for more direct comparison with MODIS data and can be used check the microwave signature of individual features of the pack and also to test the accuracy of algorithms derived from passive microwave data.

2.3 Ship Observations on board Soya

The physical characteristics of the sea ice cover in the southern portion of the Sea of Okhotsk (e.g., Ukita et al., 2000) and in other regions (Weeks and Ackley, 1986; Tucker et al., 1992) have been studied previously. The general location and details of ship observations in the Okhotsk Sea are described in Naoki et al. (2007). The enlarged version of the MODIS image shows an ice cover that is made of many ice types including those of thick first year ice, young ice, gray ice, nilas and pancake ice. It reflects the dynamic nature of the sea ice cover. The ship study is meant to complement previous studies and to make measurements that are coincident with measurements from the P3 aircraft and satellite AMSR-E observations.

The ship observation was carried out in the 100km range as shown in the general location presented in Figure 3. When the ship was moving, sea ice conditions around the ship were recorded with three camcorders installed on the mast, bow and broadside. The camcorder installed broadside measured the sea ice thickness and other physical properties of the ice. During periodic stops, ice samples and snow overlying sea ice were collected directly using a basket.

Typical observations of the ice cover during the cruise are shown in Figures 5a and 5b. In Figure 5a, rafted ice is shown in the foreground while nilas with some open water is shown in the middle part. In the background, thick ice cover covers the region up to the horizon. The image is similar to those observed from the aircraft but with more details, especially in the rafting geometry. It also represents the usual scenario following a wind forced event when new and young ice gets rafted and leads open up and turns to new ice within a few hours. The image in Figure 5b was taken on the same day but for a different part of the ice cover. In the foreground is the track of the ship that reveals

218 basically the state of the consolidated ice region. Qualitative analysis indicates that the
219 ice cover has moderate thickness and the brownish color in some floes reveals the
220 presence of algae in the underside. The presence of birds in the region indicates that it is
221 a biologically active region.
222 Thicknesses of the different types of ice cover were sampled during the and the
223 results were correlated in a separate paper (Naoki et al., 2007). The microwave signature
224 of ice of different thicknesses have been shown to be different in part because of varying
225 salinity and temperature, which were also measured during the cruise.
226
227 **3. Comparative Analysis using Concurrent Data**
228 *3.1 AMSR-E Ice Concentration versus Landsat-7 Data*
229 The most important geophysical parameter derived from passive microwave data
230 is likely sea ice concentration. It provides information about the location of the ice edge,
231 polynyas and divergence areas and is used in the estimates of the extent and area of the
232 ice cover. It can also be used to estimate how rapidly the ice advances in the winter and
233 how fast it retreats in the spring and summer. The use of Landsat-7 for process studies is
234 on the other hand very limited because of sparse coverage and the limit imposed by
235 daylight and cloud free conditions. When it is available, however, the Landsat-7 data at
236 15 m resolution provide a wealth of information about the sea ice cover (Steffen and
237 Maslanik, 1988).
238 The Landsat visible channel data presented in Figure 6a and taken on 11 February
239 2003 provides a detailed characterization of the sea ice cover in the Okhotsk Sea. The
240 albedo of sea ice in the region has been studied by Toyota et al. (1999). The image
241 indicates the complexity in the spatial distribution and composition of the ice cover at this
242 time of the year. The ice edge is characterized by the presence of ice bands as indicated
243 earlier that have been observed to consist mainly of pancake ice usually several cm to a
244 few meters in diameter. Into the ice pack, some very well defined and thick ice floes are
245 evident. These thick ice floes are likely the ones that are least altered during the ice
246 season becoming part of the consolidated ice as the grease ice between them gets totally
247 frozen. During divergent conditions, they are likely to survive as individual entities again
248 and during melt period, they are likely to be the last floes to melt in the region. The

presence of a large fraction of new ice (intermediate albedo) in the image is indicative that the region is in a rapid growth state condition. The stages include the formation tiny ice particles called frazil ice during super cooling in the upper ocean layer and the accumulation of these particles at the top surface to form what is usually called "grease ice." This ice soup solidifies to form nilas or pancake ice depending on sea surface conditions, leading to either gray ice or larger pancakes and then young ice which is about 20 to 30 cm in thickness. As the young ice gets thicker and acquires snow cover, it becomes first year ice which is the dominant ice type during the ice season. Rafting and ridging of the different ice types due to strong winds are also a natural part of the ice cover.

The availability of such concurrent images provides the opportunity to examine how the mesocale characteristics and detailed distribution of different ice types are represented in the passive microwave data. Ice concentration maps over the same general area as that in the Landsat image were derived from AMSR-E passive microwave data using the Bootstrap Algorithm in three grid formats as described earlier: (a) 6.25 km resolution using the 89 GHz (H & V) data only (Figure 6b); (b) 12.5 km resolution using the standard set of channels as described by Comiso (2004) (Figure 6c); and (c) 25 km resolution which is the standard grid for the historical data Figure 6d). It is remarkable that the basic spatial features are coherent. This is an indication that the visible and microwave sensors are sensitive to same physical characteristics of the ice cover. It is apparent that a lot of the detailed distribution of the ice cover provided by Landsat are also revealed in the AMSR-E image at 6.25 km resolution. The ice edges and divergence areas are captured by AMSR-E but not the ice bands, mainly because of lack of resolution in the latter. This implies that for a full characterization of the ice cover, visible channel data like those from Landsat-7 would be highly desired. The 12.5 km map provides a respectable representation and shows some of the divergence region while the 25 km map shows very little in terms of detail. Many of the mesoscale features that are needed for heat and humidity flux studies are thus lost in the coarse resolution images.

It is important to point out, however, that for large scale studies, the passive microwave data provide as good a representation of the ice cover as you can get. A slight

smearing of the ice edge is apparent but the maps provide consistent representation of the ice cover that is also accurate if resolution is not a factor. A quantitative comparative analysis is done using the co-registered data sets. Ice concentration is derived from Landsat-7 data within each of the AMSR-E pixel at the various grids and compared with data from the latter in Figures 7a, 7b, and 7c for AMSR-E data at 6.25, 12.5 and 25 km grid, respectively. Linear regression analysis was done on each of these plots and the regression lines are as shown. Surprisingly, however, the set of data that provided the best correlation is the 25 km data with the correlation coefficient being 0.90 while corresponding value when the 12.5 and 6.25 data sets were used are 0.97 and 0,95, respectively. The comparisons also show a large scatter of the data points with the standard deviations being about 17.14, 16.0 and 14.2 % ice concentration between Landsat data and AMSR-E data at 6.25 km, 12.5 km, and 25 km resolutions, respectively. Part of the reason for the large standard deviation is the few hours difference between the Landsat-7 coverage and the AMSR-E coverage. Thus, a slight mismatch of the location of an ice floe affects the correlation and the impact is higher with 6.25 km grid than that of the 25 km grid. The results of the comparative analysis, however, indicate that despite the relatively coarse resolution, passive microwave provides a good representation of the sea ice cover.

This also brings about the issue of what the ice concentration value, as derived from passive microwave data, really represents. Because the emissivity of sea ice varies with ice type, it is difficult to categorize the microwave footprint of ice covered areas as either ice or water. Because new ice has lower emissivities at the different frequencies and polarizations than thick ice, unless an ice typing can be done effectively, the algorithm produces ice concentrations that are lower in new ice regions than in thick ice regions. In the comparative analysis, ice concentration from Landsat was derived based on the different albedo values with the highest being 100% ice and the lowest being 100% open water. It is apparent that albedo is even more sensitive to thickness than the emissivity of sea ice.

3.2 PSR versus MODIS

The aircraft PSR data provide the means to compare data of approximately the same resolution from passive microwave and MODIS. Figure 8 shows data from MODIS and from PSR at 37 GHz(V), 18 GHz (V), 37 GHz (H), and 89 GHz (V) at the study area in the north. The MODIS data indicate that the ice cover in the region is mainly consolidated, with many large ice floes discernible, surrounded by either open water or new ice. At the top right is part of the Marginal Ice Zone (MIZ) located at the eastern part of the region (towards the Pacific Ocean, see aircraft track in Figure 1 and top right in Figure 2). The region is shown to have much lower albedo than the rest of the region, indicative of the presence of new or younger types of ice cover. The relatively elongated areas of higher albedo in the region are likely bands of pancakes and surrounded by newer ice types. Also at the top corner is a pattern suggestive of the presence of clouds that could pass by the region anytime. It is apparent that the PSR is sensitive to same general characteristics of the ice cover as the visible channel of MODIS. Except for the 89 GHz channel, a reduction in the brightness temperature in the MIZ is apparent, especially in the horizontal channel (37 GHz) which exhibits larger contrast between open ocean and ice covered areas. The 18 GHz channel also show more reduction in brightness temperature than the 37 GHz channel at vertical polarization because of the higher contrast in the emissivity of ice and water at lower frequencies. The pattern is not so obvious with the 89 GHz channel which actually shows lower brightness temperature within the pack (lower left) than the rest of the region. The aircraft went back and forth in the region to form the mosaic pattern. Gaps are shown between tracks (see Figure 1) because the aircraft was going at higher altitude than was originally planned. It took about an hour for the aircraft to make each track. The 89 GHz data for the second track (from the right) shows significantly lower brightness temperature than those of the other tracks suggesting the possibility of an atmospheric effect passing by during the hour the data were obtained. In the following track, the data apparently went back to normal.

The ice concentration algorithm was applied on the aircraft passive microwave data and the results are shown in Figure 9. It is apparent that much of the region is interpreted as basically consolidate (100%) ice with the MIZ and some leads being retrieved as having concentrations generally between 80 %(light pink) and 95 % (dark red). In this sense, the passive microwave data captures the basic characteristics of the

ice cover. Again, it does not provide complete information in that it does not capture some of the features like the presence of large floes and refrozen leads. The "tie points" for 100% ice can be adjusted in the algorithm (see Comiso, 2004) but it would depend on what type of sea ice cover would be regarded as 100% ice. This is usually not so easy to define, as indicated earlier, since during subfreezing temperatures in winter, ice can form quickly and new ice has emissivity that changes from that of open water to that of thick ice, depending on thickness.

To gain insights about the signature of the ice cover, several segments of the northern study area are shown in terms of scatter plots between different channels in Figures 10, 11, and 12. The specific segments shown in the scatter plots using of passive microwave data from the PSR are indicated by rectangular boxes in the images at the bottom. Low albedo values as determined by MODIS are plotted in red to determine how the lead areas with different thickness of new ice cover are represented in the passive microwave data. Some but limited variability is apparent at the 10, 19, and 37 GHz channels at vertical polarization while significantly greater variability is shown for 37 GHz at horizontal polarization and for 89 GHz at both polarizations. The data from the latter are especially interesting in Figure 11, suggesting that thickness information in lead areas may be possible to obtain from these channels, especially with the linear trend of the data from lead areas at the 89 GHz channels. In Figure 12, however, where a large fraction of the data is of new types of ice, the patterns do not look so linear.

The images in Figure 13 show a comparison of PSR data taken at high altitude (6000 m, when the aircraft was going north) and at low altitude (1000m, when the aircraft was going south). The data in the latter provides even improved resolution at around (50 m) when compared to those of the former. The PSR data shown is for the 37 GHz channel at horizontal resolution. It is apparent that at this resolution, much of the mesoscale features observed with the MODIS data is captured by the higher resolution PSR data. It is thus possible that if resolution is not a factor, passive microwave data can capture much of the mesoscale features that are of interest in polar process studies.

To show relationships of passive microwave data as obtained by PSR with those from AMSR-E, scatter plots of the various channels over the same ice covered regions are presented in Figure 14. The column in the left represents plots of various channels

using aircraft data while those in the right represents plots for similar channels but using AMSR-E data.

3.3. PSR versus Ship Data

The ship tract overlaid on a PSR data at 37 GHz (V) is shown in Figure 15. Ice floes along the ship tract were sampled in terms of thickness, salinity, snow cover and temperature. The brightness temperatures at all PSR channels were observed to increase quite rapidly from near zero thickness to about 10 cm thickness. Between 10 and 20 cm, the brightness temperatures also increase but more moderately. Beyond 20 cm, the change in brightness temperature with thickness was no longer discernible. The changes are more discernible with the horizontal channels than the vertical channels, which is expected because of the larger contrast in the emissivity of water and ice with the former. These information were used in conjuction with a model by Naoki et al. (2007), to show that ice thickness can be inferred from passive microwave data in new ice areas. This would be a most welcome development especially for heat flux studies.

4. Ice Types, patterns and distribution of sea ice in the Okhotsk Sea

To get a general idea about the distribution of the different types of surfaces in the Okhotsk Sea, a classification scheme was applied on the MODIS data in Figure 2a based on histograms taken in various study areas. The range of albedo for the various types were assigned arbitrarily according to what was suggested in the histogram study and we arrived at 11 classes that is displayed in different colors in Figure 16. In this scheme, thick first year ice shown in reds and the pinks represents about 37% of the Okhotsk Sea ice cover. Young ice shown as brown and yellows represents about 22 % while new ice shown in greens and blues represents about 28 % of the ice cover. Grease ice and/or open water shown in gray represent 13%. There was no validation done mainly because ship data was too limited but the qualitative representation as indicated in Figure 16 looks reasonable. If the classification is approximately right, it appears that thick ice has the highest percentage but not a dominant ice cover. This would mean that there is no

sizable core for the ice cover and the extent and area can be easily influenced by enviromental factors on a year-to-year basis.

5. Seasonal and Interannual Variability and Trends

Monitoring even just the Okhotsk Sea ice cover using concurrent ship, aircraft and satellite data on a daily basis for about 30 years would be an overwhelming talk that would require a lot of manpower and money. A more practical way is to use satellite data and ensuring that the latter are interpreted as accurately as possible. Through comparative analysis of AMSR-E ice concentration data with co-registered and concurrent Landsat and MODIS data and also PSR and ship data, we get to better understand what the ice concentration derived from passive microwave data really means. We also get a general idea about the distribution of the different ice types. We now try to use these result to interpret the seasonal and interannual variability of the sea ice cover as inferred from historical data. To make the latter relevant, we have reprocessed historical satellite data (SMMR and SSM/I) with the same technique used to process the AMSR-E data for compatibility in interpretation. During periods of overlap, the ice concentrations derived from SSM/I and AMSR-E have been shown to be very similar. The same technique were also used to process SMMR data (1978 to 1987) for a longer time series.

The most important variables that can be derived from these ice concentration maps are sea ice extent and ice area. Sea ice extent is the integrated sum of all areas with ice concentration of at least 15 % while ice area is the integrated sum of the product of the area and the ice concentration over all ice covered regions. The daily ice extents and monthly ice anomalies are presented in Figure 17 while the daily ice areas and monthly ice area anomalies are presented in Figure 18. The daily extents show the yearly seasonality of the sea ice cover and how this has varied over the past 28 years. There is apparently a large interannual variability in the yearly peak values with lows in 1984, 1991, 1997 and 2006 and highs in 1979, 1988, and 2001. Because of large seasonal variability, trends in the ice cover are difficult to infer from the daily data. A more standard procedure is to subtract the climatology based on the interannual average of all available data for each month (e.g., Bjorgo et al., 1997; Cavalieri et al., 1997). The monthly ice extent anomalies as presented in Figure 17b show large positive anomalies in

433 the late 1970s and early 1980s and some negative anomalies in the last 3 years.
434 Regression analysis using this data yielded a trend in ice extent of -8.8% per decade.
435 Such a trend is quite substantial considering that the overall trends for the entire Arctic
436 region is about -3% per decade (Parkinson et al., 1999). Similar analyses using ice area
437 as defined earlier are presented in Figures 18a and 18b. The overall trend in the ice area
438 is even greater at -12.0 % per decade. Such trend is quite alarming and indicates that the
439 Sea of Okhotsk is even more vulnerable in loosing its ice cover than the perennial ice
440 cover in the Arctic as reported in Comiso (2002), and Stroeve et al.(2004) and updated in
441 Comiso (2006). To gain insights into this trend, the length of each ice season from 1979
442 to the present were inferred from daily data and the results are presented in Figure 19.
443 The trend is more modest showing declines of about 2 to 4 days per decade. The latter
444 may not mean much because the ice cover is seasonal ice and it takes only subfreezing
445 temperatures to create sea ice. The region is usually below freezing during the winter
446 period. An early or late start date is therefore not as significant as the observed decline
447 in ice extent and ice area since the latter suggest warmer winter temperatures. It is
448 warmer winter temperatures that could lead to lower rate of freeze-up which means less
449 extensive ice cover. There are other complications including the composition of the ice
450 cover as discussed in the next section.
451
452
453 **6. Discussion and Conclusions**
454 The Sea of Okhotsk has the potential of providing an important signal about the
455 changing global climate since it is the southernmost region in the Northern Hemisphere
456 with an ice cover. We have been using passive microwave ice concentration data to
457 monitor the ice cover in the region but the latter is difficult to interpret especially in a
458 very divergent and rapidly changing environment like the Sea of Okhotsk. In this study,
459 we examined the general physical and radiative characteristics of the sea ice cover in the
460 Okhotsk Sea using concurrent in situ, aircraft and satellite data. High resolution satellite
461 data reveal a complex distribution of the ice cover with only about 37% being covered by
462 thick ice types and the rest being young and new ice, the signature of which can be very
463 unpredictable. They show many complex features in the ice cover that cannot be

represented in the standard passive microwave data sets. With data from the recently launched AMSR-E sensor, many of such mesoscale features are adequately represented, especially in the 89 GHz images, making the latter a useful tool for polar process studies. However, the data has to be used with care since data at this wavelength is sensitive to atmospheric and snow cover effects. The standard sea ice data from passive microwave at 12.5 km resolution shows some of the mesoscale features as well but much of the features are lost in the 25 km grids. Our results, however, show that the 25 km grid provides dependable ice cover data that can be combined with historical data to study the state and future of the ice cover.

The results of our analysis of historical data show that the sea ice cover in the Okhotsk Sea is declining at a rapid rate of -8.8 and -12.0 % per decade for sea ice extent and ice area, respectively. Such trend is alarming especially since the region is a very productive region in part because of the presence of sea ice. Since the Okhotsk Sea ice cover has a relatively small fraction of thick ice (about 37%) and the average concentration of ice in the Okhotsk Sea is about 90%, a large fraction of the consolidated ice consists of young and new ice. The ice cover has actually declined in a similar way in the 1990s. The lack of a strong dependable core of thick ice that provides stability in the ice cover could mean that the year-to-year variability can easily be attributed by environmental forcing such as wind strength and direction during winter and spring. The higher decline in ice area compared to that of the ice extent also indicates that the region is getting more divergent with the average concentrations getting lower with time. What this implies in the context of a warming Arctic is not known and will be the subject for future studies. What we know is that the length of the ice season has been declining but only by about 2 to 4 days per decade. Such change is not sufficient to explain the high rate of decline since the entire region is in sub-freezing temperatures during the winter months. Further studies are needed especially since the observed high rate of decline in ice extent and ice area may mean that the rate of ice production in the region is declining on account of a warmer winter.

Table 1. AMSR-E Sensor Characteristics

Freq. GHz) Wavelength	6.9 4.3 cm	10.65 2.8 cm	18.7 1.6 cm	23.8 1.27 cm	36.5 0.82 cm	89.0 0.34 cm
Polarization	H & V	H & V	H & V	H & V	H & V	H & V
IFOV (km)	73.0x43.1	49.8x29.6	26.2x16.5	30.8x19.0	13.7x10.3	6.0x4.9
Mean Res. (km)	56	38	21	24	12	5.4
Sens (K)	0.3	0.6	0.6	0.6	0.6	1.1
Int. time (msec)	2.6	2.6	2.6	2.6	2.6	1.3
Beamwidth (°)	2.2	1.4	0.8	0.9	0.4	0.18
Swath Width	1445 km					
Satellite Altitude	705 km					

References

Alfultis, M.A. and S. Martin, Satellite passive microwave studies of the Sea of Okhotsk ice cover and its relation to oceanic processes, 1978-1982, *J. Geophys. Res., 92*, 13,013-13,028, 1987.

Bjorgo, E. , O.M. Johannessen, and M.W. Miles, "Analysis of merged SSMR-SSM/I time series of Arctic and Antarctic sea ice parameters 1978-1995," *Geophys. Res. Lett.*, Vol. 24, pp. 413-416, 1997.

Cavalieri, D.J., P. Gloersen, W.J. Campbell, Determination of sea ice parameters with the Nimbus7 SMMR, *J. Geophys Res., 89,* 5355-5369, 1984.

Cavalieri, D.J., P. Gloersen, C. Parkinson, J. Comiso, and H.J. Zwally, Observed hemispheric asymmetry in global sea ice changes, *Science, 278*(7), 1104-1106,1997.

Comiso, J. C., Characteristics of winter sea ice from satellite multispectral microwave observations, *J. Geophys. Rev., 91*(C1), 975-994, 1986.

511 Comiso, J. C., A rapidly declining Arctic perennial ice cover, *Geophys Res. Letts.,*
512 *29(20), 1956, doi:10.1029/2002GL015650,* 2002.
513 Comiso, J.C., Sea ice algorithm for AMSR-E, *Rivista Italiana di Telerilevamento (Italian*
514 *Journal of Remote Sensing), 30/31*, 119-130, 2004.
515 Comiso, J. C., Abrupt Decline in the Arctic Winter Sea Ice Cover, *Geophys. Res. Lett.,33,*
516 L18504, doi:10.1029/2006GL027341, 2006.
517 Comiso, J. C., D. J. Cavalieri, and T. Markus, Sea ice concentration, ice temperature, and
518 snow depth, using AMSR-E data, *IEEE TGRS, 41(2),* 243-252, 2003.
519 Matzler, C., R. O. Ramseier, and E. Svendsen, "Polarization effects in sea ice
520 signatures," *IEEE J. Oceanic Engineering*, Vol. OE-9, pp. 333-338, 1984.
521 Naoki, K. J. Ukita, F. Nishio, M. Nkayama, J. Comiso and A. Gasiewski, Thin sea ice
522 thickness as inferred from passive microwave and in situ observations, J. Geophys.
523 Res. (2007, submitted).
524 Nishio, F. M. Aota, and K. Cho, Variability of se ice extent in the Okhotsk Sea,
525 *Proceedings of the Sea of Okhotsk Symposium,* pp. 1-4, 1998.
526 Parkinson, C.L., D.J Cavalieri, P. Gloersen, H.J. Zwally, and J.C. Comiso, Arctic sea ice
527 extents, areas, and trends, 1978-1996, *J. Geophys. Res.*, *104*(C9), 20837-20856, 1999.
528 Steffen, K. and J.A. Maslanik, Comparison of Nimbus 7 Scanning Multichannel
529 Microwave Radiometer radiance and derived sea ice concentrations with Landsat
530 imagery for the north water area of Baffin Bay, *J. Geophys. Res., 93(C9),* 10,760-
531 10,781, 1988.
532 Stroeve, J.C., M.C., Serreze, F. Fetterer, T. Arbetter, M. Meier, J. Maslanik and K.
533 Knowles, Tracking the Arctic's shrinking ice cover: Another extreme September
534 minimum in 2004, *Geophys. Res. Lett. 32*, doi:10.1029/2004GL021810, 2004.
535 Svendsen, E., C. Matzler, T.C. Grenfell, "A model for retrieving total sea ice
536 concentration from a spaceborne dual-plarized passive microwave instrument
537 operating near 90 GHz," *Int. J. Rem. Sens.*, Vol. 8, pp. 1479-1487, 1987.
538 Swift, C.T., L.S. Fedor, and R.O. Ramseier, An algorithm to measure sea ice
539 concentration with microwave radiometers, *J. Geophys. Res., 90(C1)*, 1087-1099,
540 1985.
541 Toyota, T. , J. Ukita, K.I. Ohshima, M. Wakatsuchi and K. Muramoto, A measurement of

sea ice albedo over the southwestern Okhotsk Sea, *J. Meteor. Soc. Japan, 77,* 117-133, 1999.

Tucker, W.B., D.K. Perovich, and A.J. Gow, "Physical properties of sea ice relevant to remote sensing," Chapter 2, *Microwave Remote Sensing of Sea Ice*, (ed. by Frank Carsey), American Geophysical Union, Washington, D.C., 9-28, 1992.

Ukita, J., T. Kawamura, N. Tanaka, T. Toyota, and M. Wakatsuchi, Physical and stable isotopic properties and growth processes of sea ice collected in the southern Sea of Okhotsk, *J. Geophys. Res., 105,* 22083-22093, 2000.

Vant, M.R., R.B. Gray, R.O. Ramseier, and V. Makios. 1974. Dielectric properties of fresh and sea ice at 10 and 35 GHz, *J. Applied Physics*, *45(11)*, 4712-4717.

Weeks, W.F., and S. F. Ackley, The growth, structure and properties of sea ice, *The Geophysics of Sea Ice,* edited by N. Unterstiener, pp. 9-164, *NATO ASI Ser.B*, vol. 146, Plenum, New York, 1986.

List of Figures

Figure 1. AMSR-E ice concentration map of the Okhotsk Sea showing the P3 aircraft track on 7 February 2003.

Figure 2. MODIS image of the Okhotsk Sea ice cover on 7 February 2003 in the (a) visible and (b) infrared channels with general locations of coastal and sensible heat polynya.

Figure 3. Enlarged MODIS image of the Okhotsk Sea ice cover on 7 February 2003 in the (a) visible and (b) infrared channels.

Figure 4. Aerial photograph of (a) new ice and (b) thick ice floes in the Okhotsk Sea on 7 February 2003 as taken from the P3 aircraft.

Figure 5. Typical sea ice cover of (a) rafted ice and grease ice and (b) broken thick ice as observed from the ship

Figure 6. Landsat-7 visible channel data and AMSR-E ice concentration images using (a) 6.25 km; (b) 12.5 km; and (c) 25 km resolution data.

Figure 7. Scatter plots of Landsat-7 versus AMSR-E data at a resolution of (a) 6.25 km; (b) 12.5 km; and (c) 25 km.

572 Figure 8. MODIS image in the northern region and corresponding PSR data at 37
573 GHz(V), 18 GHz (V), 37 GHz (H), and 89 GHz (V).
574 Figure 9. PSR data converted to ice concentration and corresponding MODIS data.
575 Figure 10. Scatter plots of 10 GHz (V) versus 37 GHz (V); 19 GHz (V) vs 37 GHz (V);
576 37 GHz (H) vs 37 GHz (V) and 89 GHz (H) vs 89 GHz (V). The red data points
577 represent low albedo areas inside the box in the image below the plots. The box is in a
578 divergence region.
579 Figure 11. Scatter plots of 10 GHz (V) versus 37 GHz (V); 19 GHz (V) vs 37 GHz (V);
580 37 GHz (H) vs 37 GHz (V) and 89 GHz (H) vs 89 GHz (V). The red data points
581 represent low albedo areas inside the box in the image below the plots. The box is in a
582 consolidated ice region.
583 Figure 12. Scatter plots of 10 GHz (V) versus 37 GHz (V); 19 GHz (V) vs 37 GHz (V);
584 37 GHz (H) vs 37 GHz (V) and 89 GHz (H) vs 89 GHz (V). The red data points
585 represent low albedo areas inside the box in the image below the plots. The box is in the
586 marginal ice zone.
587 Figure 13. MODIS image and PSR data at high (6000m) and low (1000m) altitudes with
588 the latter showing even higher resolution than MODIS data.
589 Figure 14. Scatter plots comparing aircraft data with AMSR-E data
590 Figure 15. Ship track on the PSR data on 7 February 2003
591 Figure 16. Ice class map using MODIS visible channel data. Red and pink represent
592 thick ice, brown and yellow represent young ice, while green and blues represent new ice.
593 Gray represents either grease ice or open water.
594 Figure 17. (a) Seasonal and interannual variability of the ice extent of the Sea of Okhotsk
595 and Sea of Japan; (b) Anomalies and trends in the ice extent of the Sea of Okhotsk ice
596 cover
597 Figure 18. (a) Seasonal and interannual variability of the ice area of the Sea of Okhotsk
598 and Sea of Japan; (b) Anomalies and trends in the ice area of the Sea of Okhotsk ice
599 cover.
600 Figure 19. Length of the ice season in the Okhotsk Sea from 1978 to 2005 (blue) and the
601 width at half-height of the plots in Figure 18a.
602

603
604

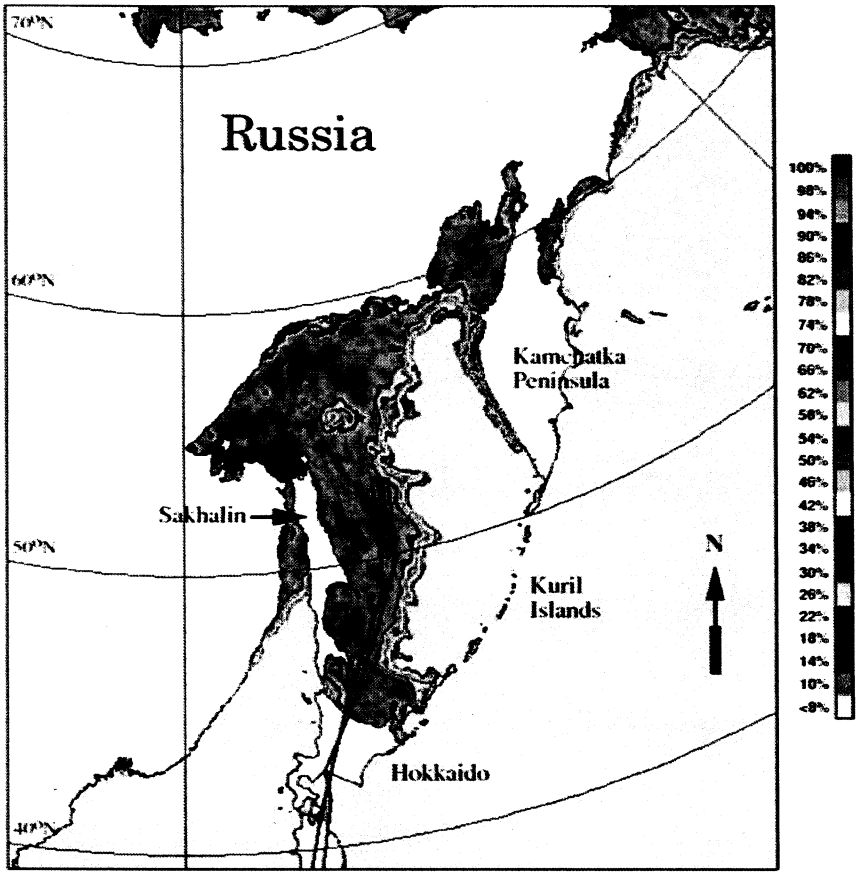

605
606
607
608
609 Figure 1 AMSR-E ice concentration map of the Sea of Okhotsk on 7 February 2003 and flight track of the
610 aircraft mission on the same day.

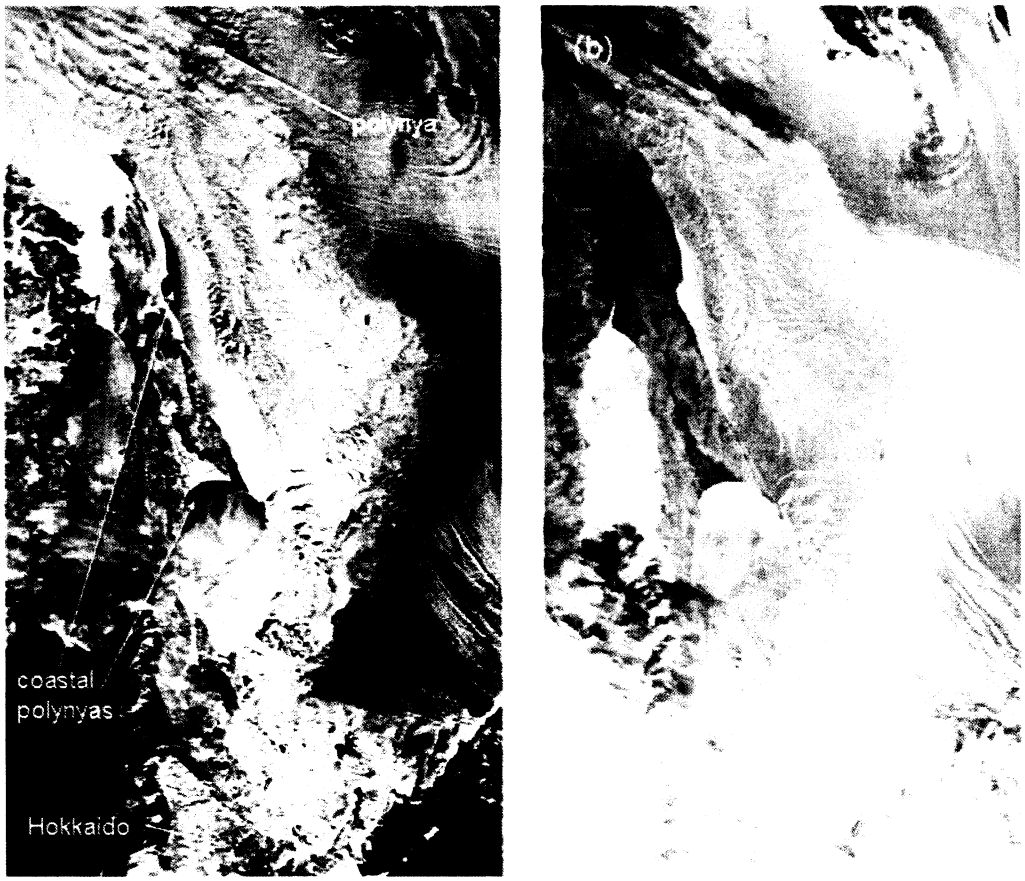

611
612
613
614 Figure 2. MODIS image of the Okhotsk Sea ice cover on 7 February 2003 in the (a)
615 visible (6 μm) and (b) thermal infrared (11 μm) channels of Aqua/MODIS sensor.
616
617

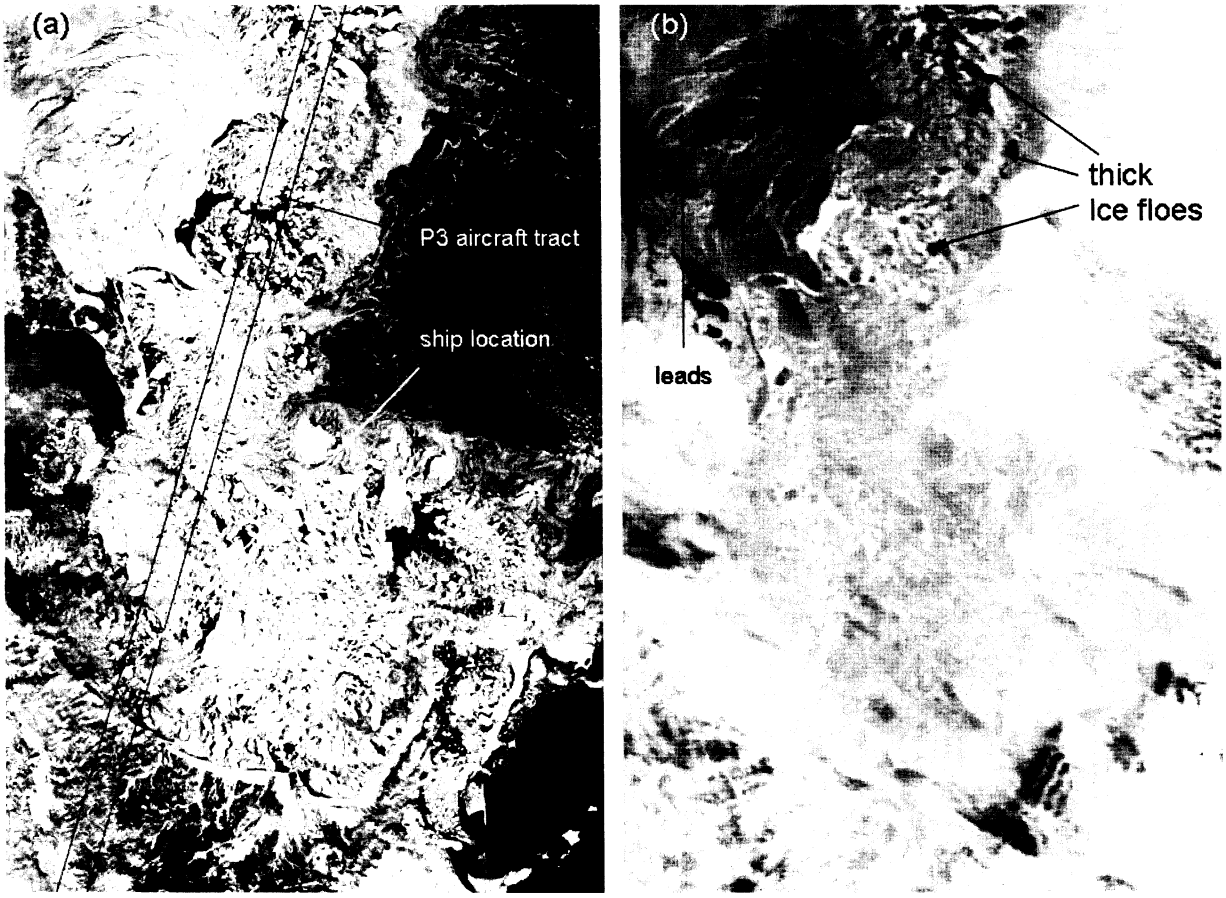

618
619
620
621 Fig. 3 Enlarged MODIS image of the Okhotsk Sea ice cover in the (a) visible (6 μm)
622 and (b) thermal infrared (11 μm) channels of Aqua/MODIS sensor.
623
624

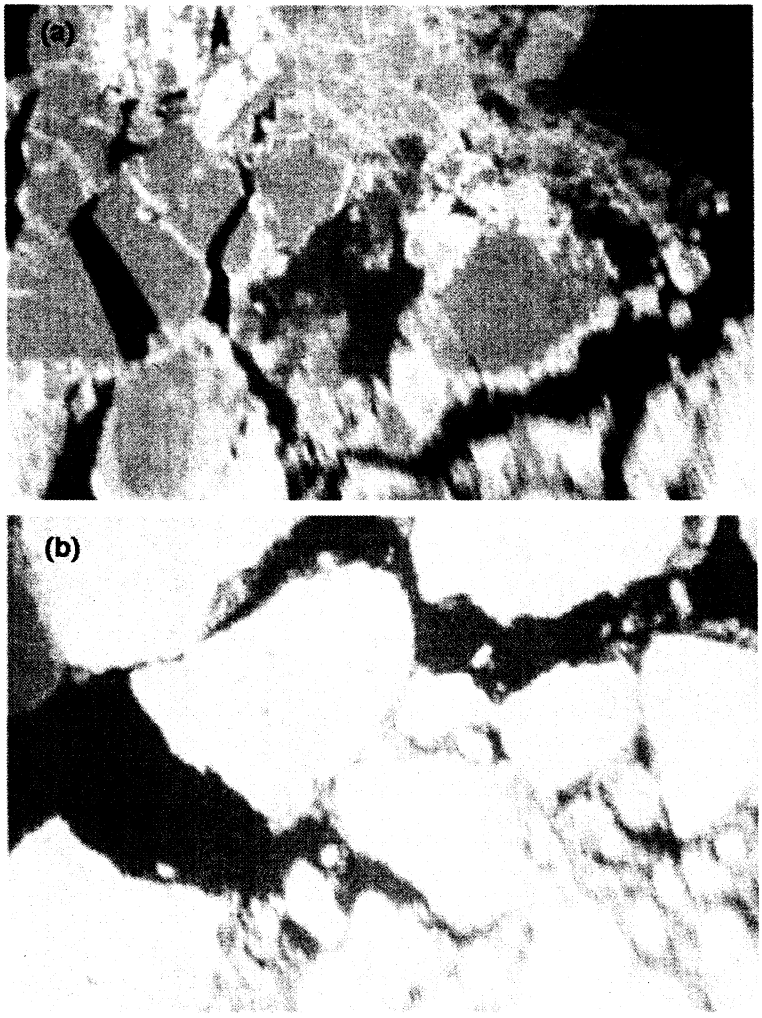

625
626 Figure 4. Typical (a) new ice and (b) thick ice floes in the Okhotsk Sea as viewed from the P3
627 Aircraft
628
629
630

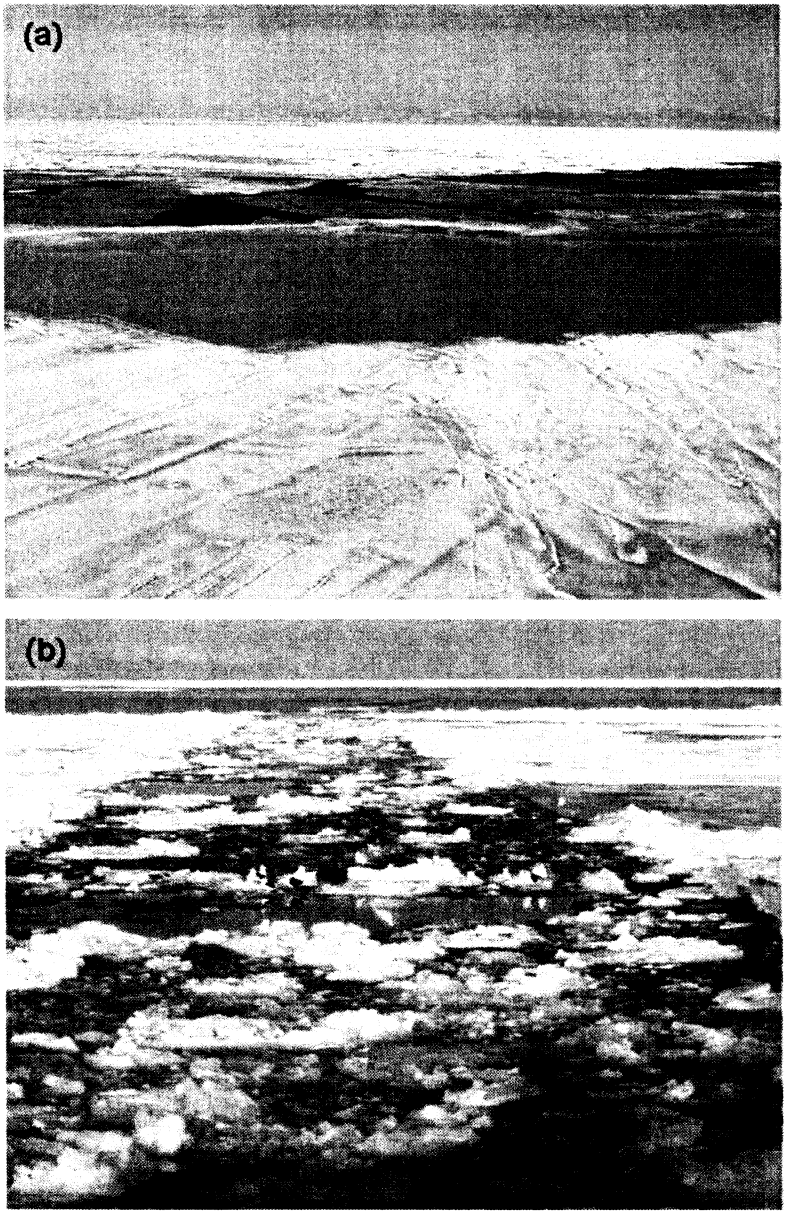

631
632
633 Figure 5. Sample photographs of sea ice from ship of (a) rafted and grease ice; and (b) broken thick
634 ice in the Okhotsk Sea
635

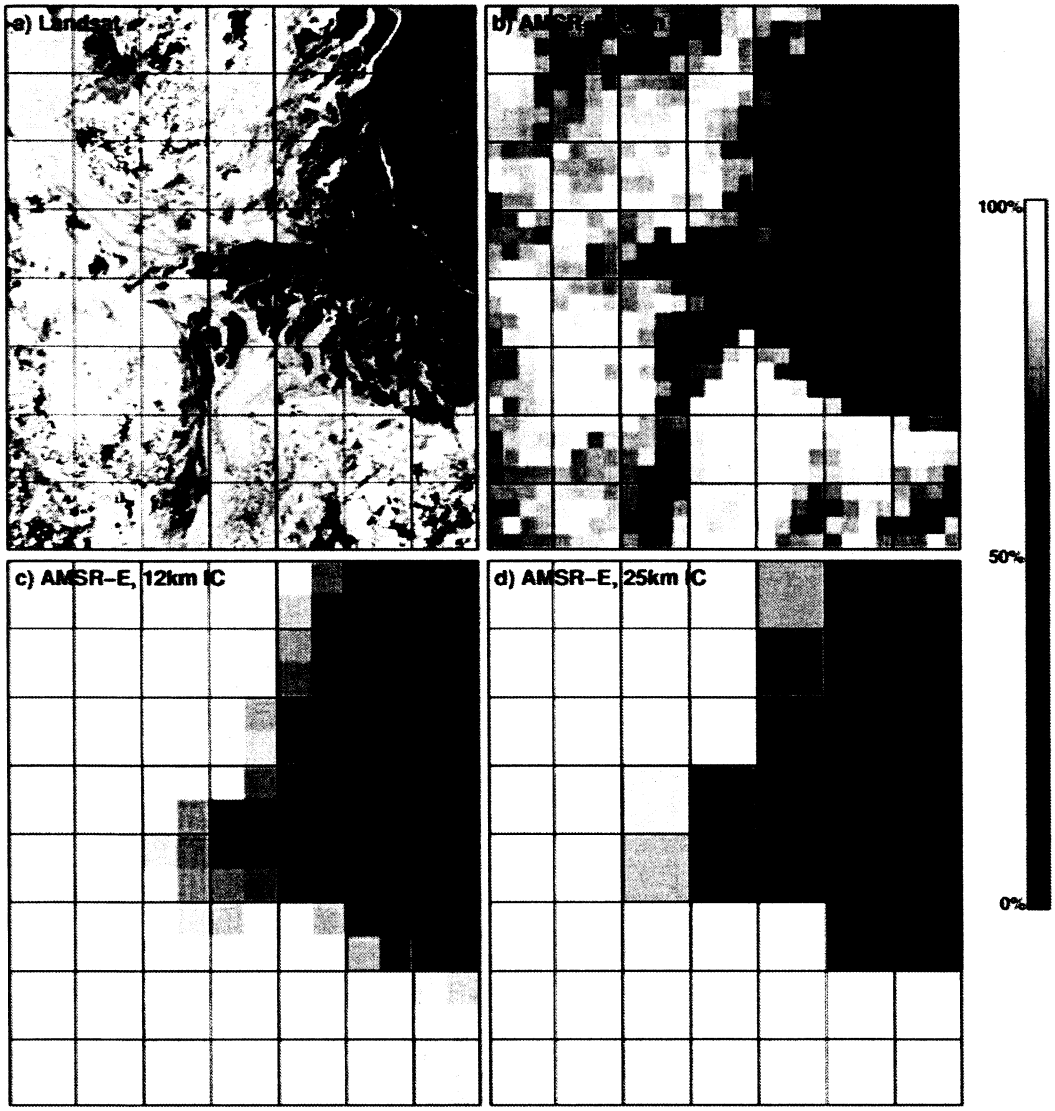

Figure 6 Landsat-7 image of the Okhotsk Sea ice cover and corresponding AMSR-E ice concentration map at the (a) 6.25 km grid; (b) 12.5 km grid; and (c) 25 km grid.

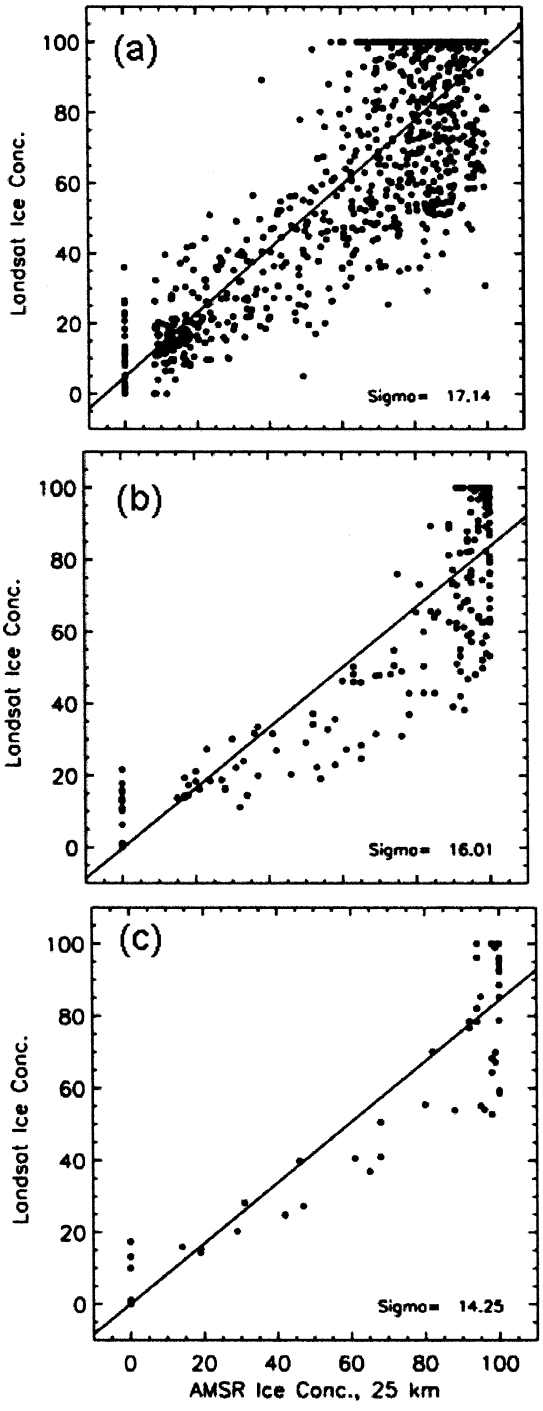

641
642
643
644 Figure 7. Scatter plots of Landsat-7 ice concentration versus AMSR-E data at the (a)
645 6.25 km grid; (b) 12.5 km grid; and (c) 25 km grid.
646

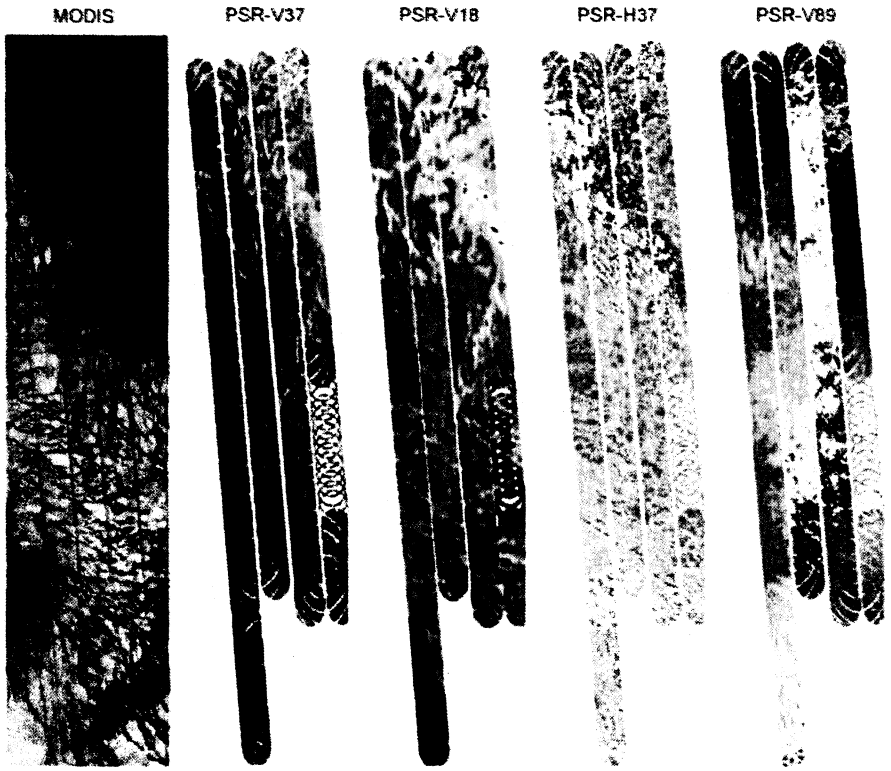

647
648
649 Figure 8. MODIS image in the northern region and PSR data at 37 GHz(V), 18 GHz (V),
650 37 GHz (H) and 89 GHz (V).
651

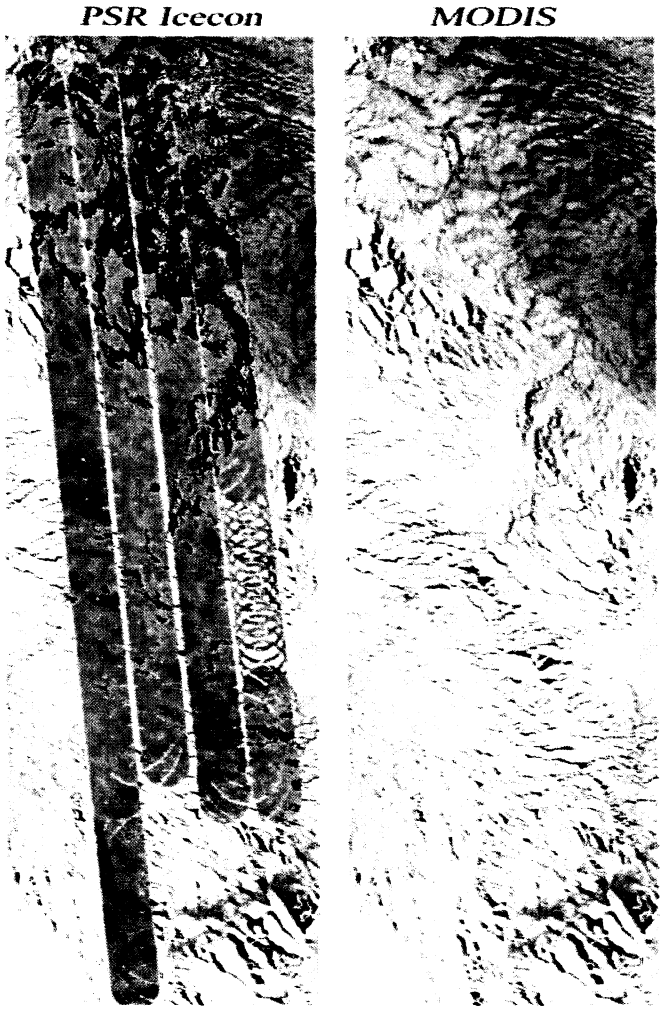

652
653 Figure 9. PSR ice concentration data (in color) derived using the Bootstrap Algorithm
654 and MODIS data (in black and white). Color scale is the same as in Figure 1.

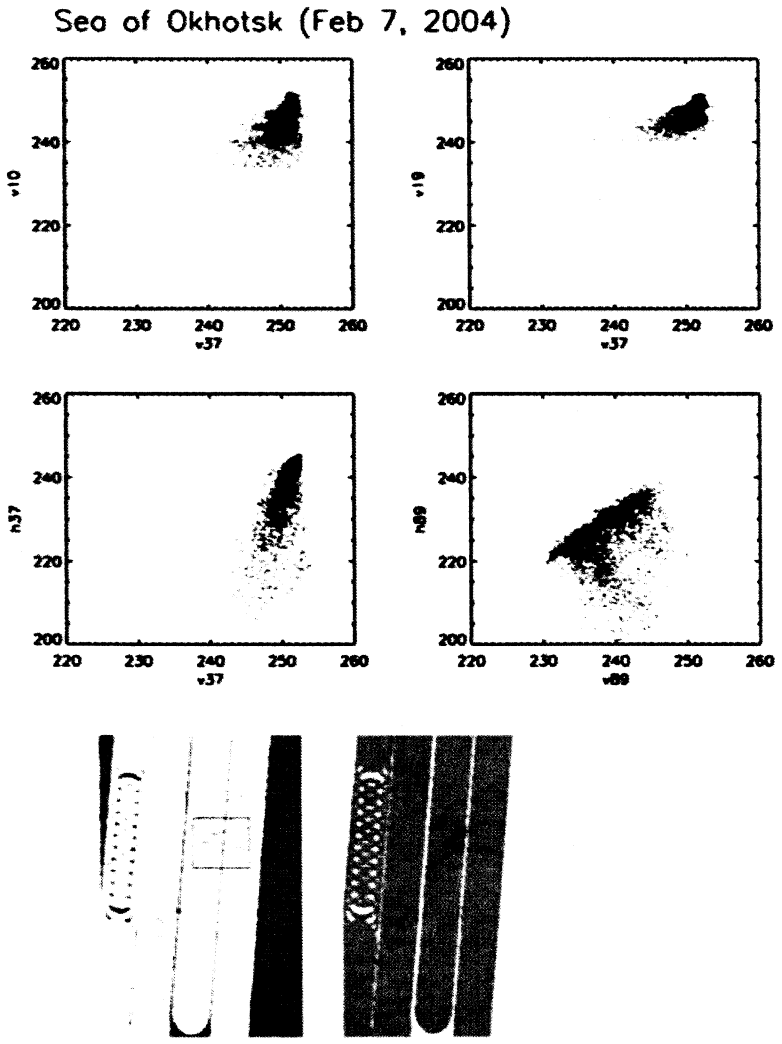

Figure 10. Scatter plots of 10 GHz (V) versus 37 GHz (V); 19 GHz (V) vs 37 GHz (V); 37 GHz (H) vs 37 GHz (V) and 89 GHz (H) vs 89 GHz (V). The red data points represent low albedo areas inside the box in the image below the plots. The box is in a divergence region.

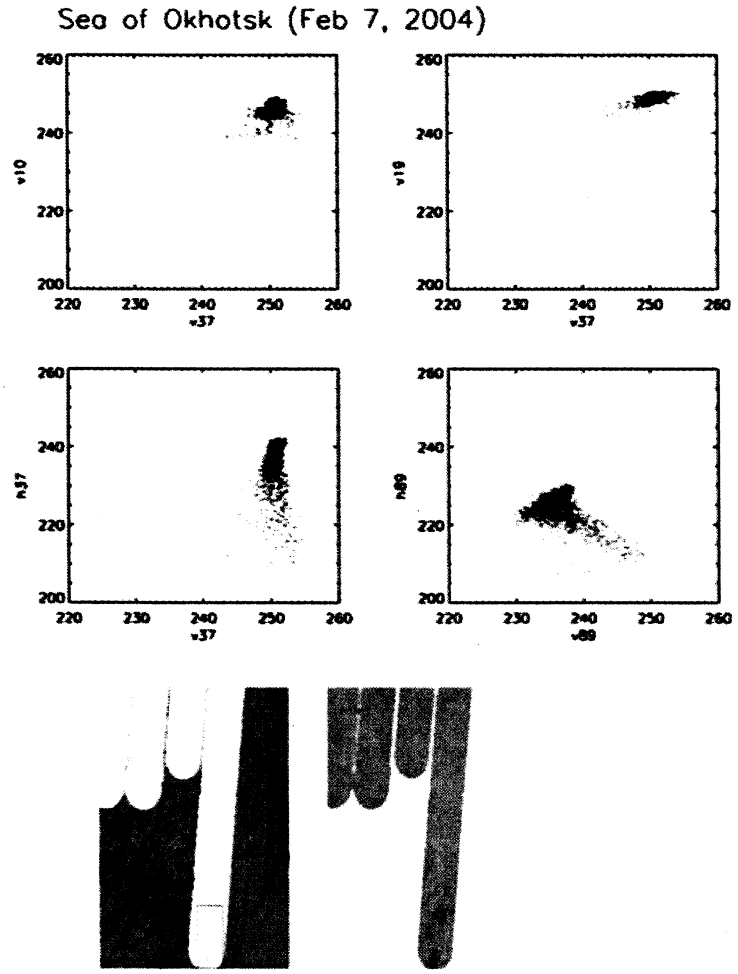

Figure 11. Scatter plots of 10 GHz (V) versus 37 GHz (V); 19 GHz (V) vs 37 GHz (V); 37 GHz (H) vs 37 GHz (V) and 89 GHz (H) vs 89 GHz (V). The red data points represents low albedo areas inside the box in the image below the plots. The box is in a consolidated ice area.

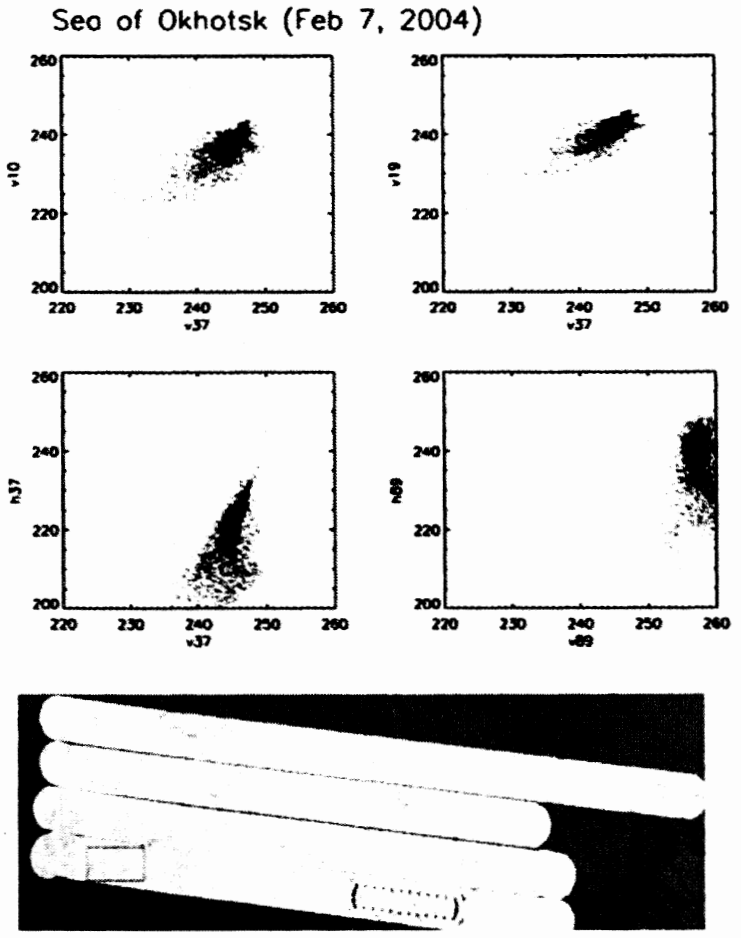

Figure 12. Scatter plots of 10 GHz (V) versus 37 GHz (V); 19 GHz (V) vs 37 GHz (V); 37 GHz (H) vs 37 GHz (V) and 89 GHz (H) vs 89 GHz (V). The red data poits represents low albedo areas inside the box in the image below. The box is in a marginal ice zone region.

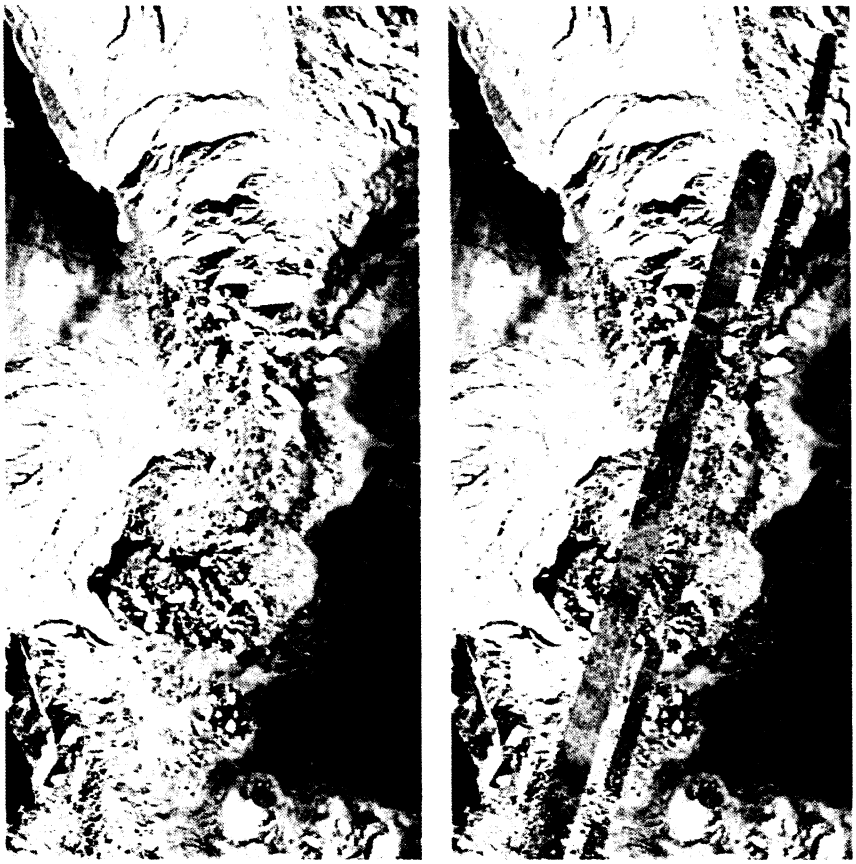

675
676
677 Figure 13. (b) MODIS image over the Okhotsk Sea on 7 February 2003; and (b) MODIS
678 image with PSR high (6000 m) and low altitude (1000 m) data at 37 GHz over Okhotsk
679 Sea.

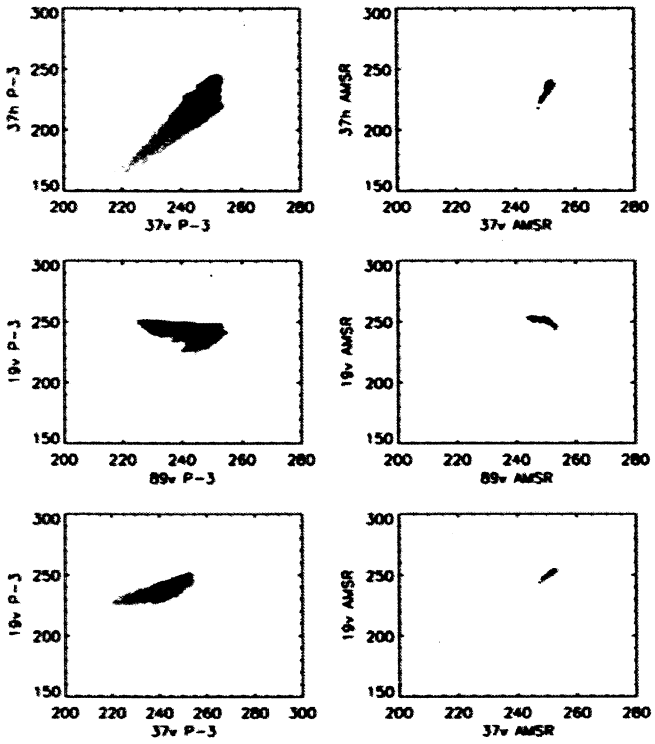

Figure 14 Scatter plots comparing PSR and AMSR-E data

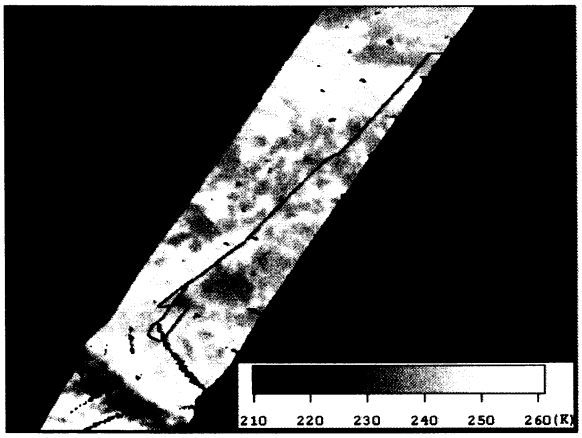

Figure 15. Ship track on the PSR data on 7 February 2003

Figure 16. Ice class map using MODIS visible channel data. Red and pink represent thick ice, brown and yellow represent young ice, while green and blues represent new ice. Gray represents either grease ice or open water.

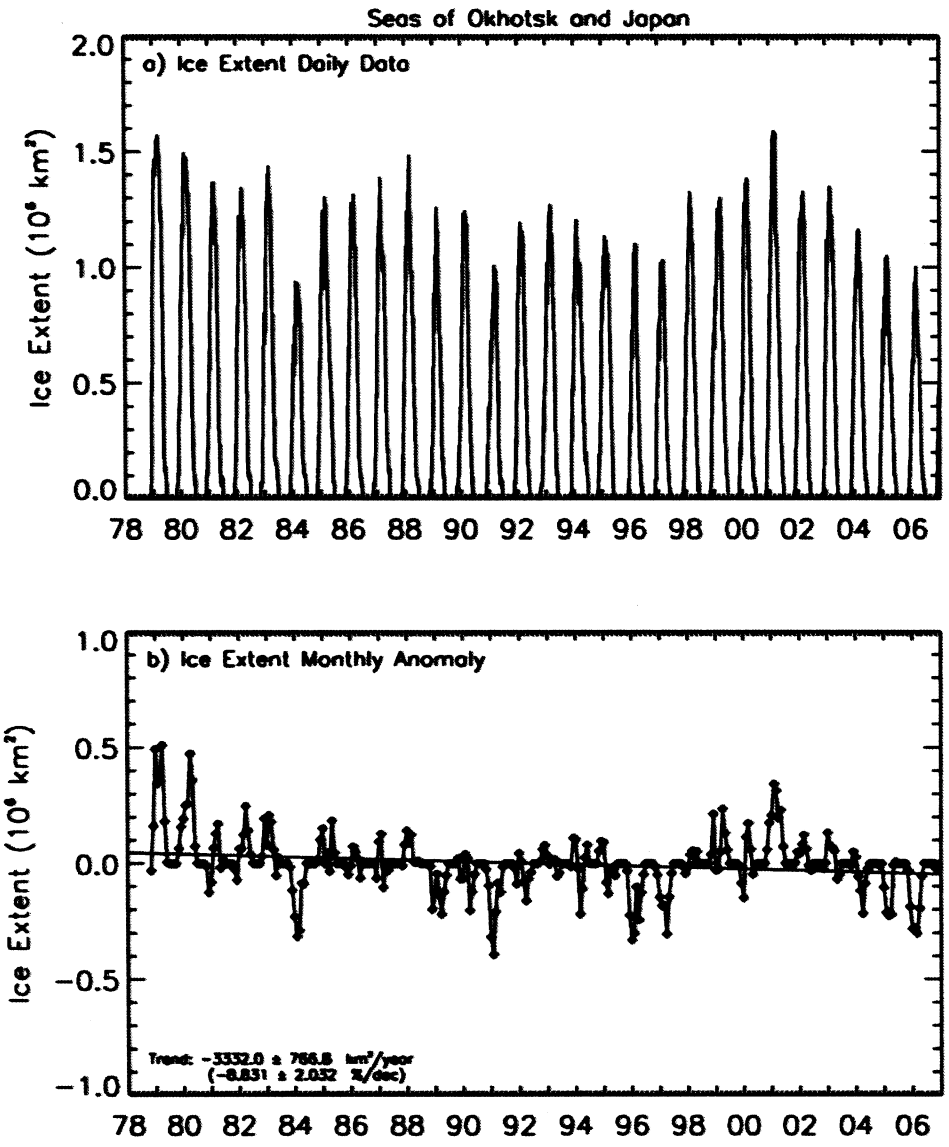

Figure 17. (a) Seasonal and interannual variability of the ice extent of the Sea of Okhotsk and Sea of Japan from 1978 to 2006; (b) Anomalies and trends in the ice extent of the Sea of Okhotsk ice cover from 1978 to 2006.

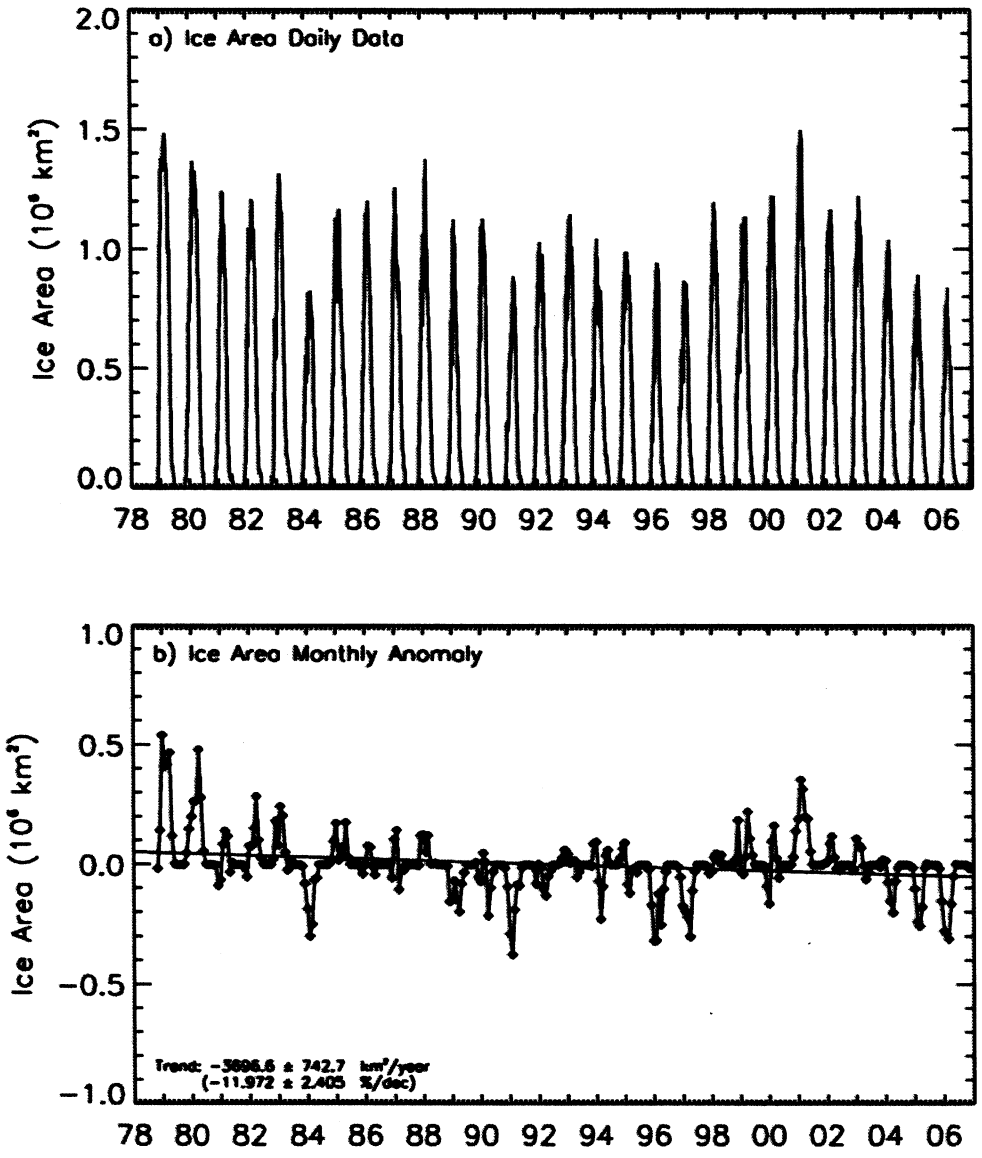

699
700
701 Figure 18. (a) Seasonal and interannual variability of the ice area of the Sea of Okhotsk
702 and Sea of Japan from 1978 to 2006; and (b) Anomalies and trends in the ice area of the
703 Sea of Okhotsk ice cover from 1978 to 2006.
704

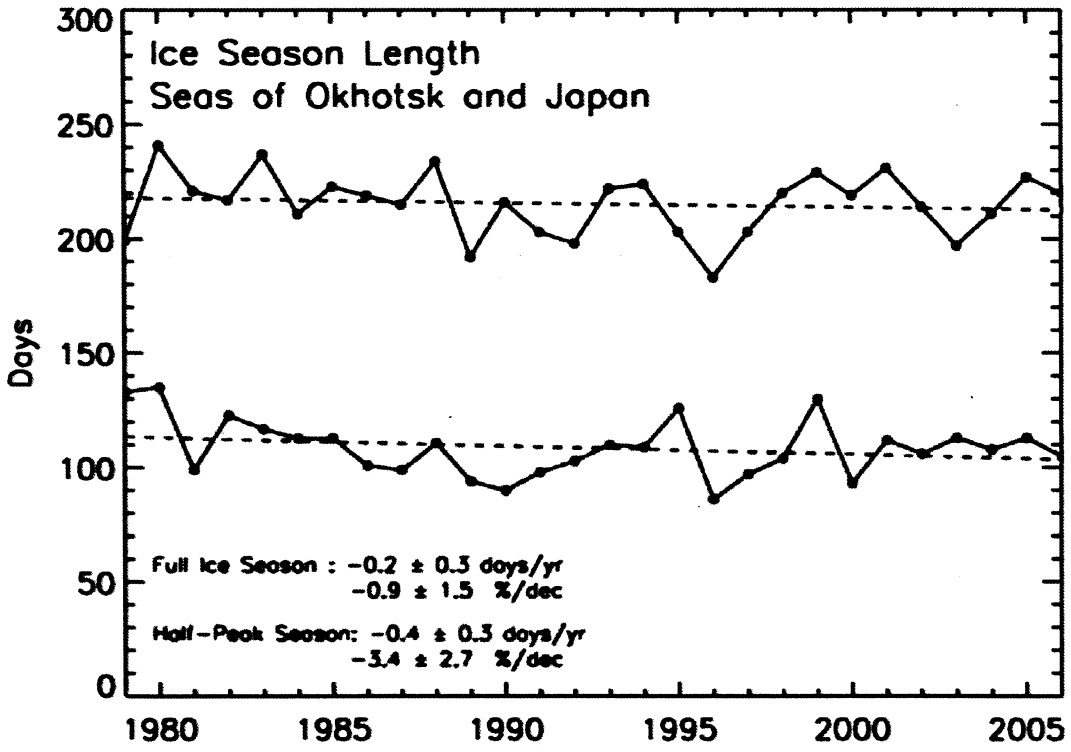

705
706 Figure 19. Length of the ice season in the Okhotsk Sea from 1978 to 2005 (blue) and the
707 width at half-height of the plot in Figure 18a.